Applied Surface Science 546 (2021) 149033

Contents lists available at ScienceDirect

Applied Surface Science

journal homepage: www.elsevier.com/locate/apsusc

Full Length Article

Effect of SILAR-anchored $ZnFe_2O_4$ on the $BiVO_4$ nanostructure: An attempt towards enhancing photoelectrochemical water splitting

Sutripto Majumder [a,*], Nguyen Duc Quang [a], Truong Thi Hien [a], Nguyen Duc Chinh [a], Nguyen Manh Hung [a,b], Haneul Yang [a], Chunjoong Kim [a,*], Dojin Kim [a,*]

[a] Department of Materials Science and Engineering, Chungnam National University, Daejeon 34134, Republic of Korea
[b] Department of Materials Science and Engineering, Le Quy Don Technical University, Hanoi 100000, Viet Nam

ARTICLE INFO

Keywords:
Successive ionic layer adsorption and reaction
$BiVO_4/ZnFe_2O_4$
Heterojunction
Photoelectrochemical
Water splitting

ABSTRACT

Development of high performance photoanodes for application in solar-driven photoelectrochemical cells is considered a grand challenge. Various structures and materials have been studied to overcome the current performance limit of the photoanode in photoelectrochemical cells; however, the enhancement in both stability and photocurrent has not been realized to date. In our study, the successive ionic layer adsorption and reaction method is used to coat $ZnFe_2O_4$ nanoparticles on the $BiVO_4$ photoanodes. Various characterizations about structural, morphological, and optical characterizations confirm the presence of anchored $ZnFe_2O_4$ nanoparticles over $BiVO_4$. Showing remarkable stability, the photocurrent density of optimized $BiVO_4/ZnFe_2O_4$ is significantly increased compared with that of the bare $BiVO_4$ nanostructured thin film. Mott-Schottky and electrochemical impedance spectroscopy analyses demonstrate that the appropriate number of the successive ionic layer adsorption and reaction cycles leads to efficient charge transfer. Furthermore, the correlation among structural, morphological and optical properties is discussed here.

1. Introduction

Currently, energy production from the environmentally friendly sources is highly attractive to resolve the global energy and environmental issues resulting from the abuse of fossil-based resources. Among various strategies, photoelectrochemical (PEC) water splitting using solar energy is of great interest, which produces oxygen and hydrogen at the photoanode and photocathode, respectively. In order to design the PEC cell with high water splitting efficiency, the fabrication of the high-performance photoanode is most challenging due to the sluggish reaction kinetics for the oxygen evolution reaction followed by the high overpotential at the photoanode. As a photoanode, the material should have optimum band gap to effectively absorb the sun light, compatible with redox potential, facile charge transfer ability, and stable in aqueous solution [1]. To date, materials including TiO_2,[2] WO_3,[3] Fe_2O_3,[4] ZnO,[5] C_3N_4,[6] $SrTiO_3$,[7] and so on have been intensively studied for the photoanode materials, but their photoelectrochemical performances were not satisfactory to achieve high efficiency required for industrial level.

Recently, $BiVO_4$ with the monoclinic structure is considered a good candidate for use in the PEC anode [8–10]. This complex metal oxide has optimum energy positions of conduction and valence band edges toward oxidation of oxygen,[11] while the optical band gap is 2.3–2.6 eV, ensuring the effective absorption of visible light [8]. In addition, $BiVO_4$ is nontoxic and naturally abundant. Indeed, most successful operation of the photoanode has been reported in $BiVO_4$ [12]. Despite its attractive characteristics, the PEC performance of the bare $BiVO_4$ has been limited due to its slow charge transport [13]. To enhance the charge transport properties in $BiVO_4$, doping with aliovalent cations,[14] formation of heterojunctions,[15] and addition of oxygen-evolving catalysts (OECs) [16] have been studied so far.

Moniz *et al.* reported that the heterojunction is one of the most successful strategies, which enables facile charge transport followed by enhanced PEC performance by built-in electrical field in the junction [17]. Among the various heterojunction types, the staggered band alignment (type-II) is most effective for the increase in PEC water splitting performance considering the opposite flows of electrons and holes. Therefore, many studies have been devoted to the formation of type II heterostructures including $BiVO_4/Fe_2O_3$, $BiVO_4/TiO_2$, $BiVO_4$/ZnO, $BiVO_4/SnO_2$, $BiVO_4$/ Ag_3PO_4, $BiVO_4$/CuSCN, etc. [13,18–22] The

* Corresponding authors.
E-mail addresses: smajumder_83@cnu.ac.kr (S. Majumder), ckim0218@cnu.ac.kr (C. Kim), dojin@cnu.ac.kr (D. Kim).

https://doi.org/10.1016/j.apsusc.2021.149033
Received 6 November 2020; Received in revised form 21 December 2020; Accepted 11 January 2021
Available online 20 January 2021

selection of the proper material for the heterojunction with $BiVO_4$ is very important to achieve the high PEC performance.

$ZnFe_2O_4$ with the spinel structure can be one of the candidates since $ZnFe_2O_4$ reveals a favorable band gap of 1.86 eV as well as the optimum location of the conduction and valence bands for the type-II heterojunction with $BiVO_4$. Furthermore, zinc ferrite is stable under the wide range of pH and it is environmental benign and naturally abundant. Therefore, $ZnFe_2O_4$ has been studied to construct the appropriate junction with different materials such as TiO_2, ZnO, Fe_2O_3, and so on [23–25]. The $BiVO_4/ZnFe_2O_4$ hetero-nanostructure was reported, which showed better PEC stability compared with bare $BiVO_4$ [26]. However, $ZnFe_2O_4$ has attracted little attention because it could improve the stability of $BiVO_4$ only with the high pH electrolyte [27]. Considering favorable characteristics of $ZnFe_2O_4$ as the counterpart of the $BiVO_4$-based heterojunction, the better physicochemical stability of the heterojunction enables the more effective nanostructure for the photo-anodic reaction. Recently, the successive ionic layer adsorption and reaction (SILAR) process has been reported, which could utilize ions as building blocks to form nanostructured thin films [28]. The nanostructures of the material can be easily tuned by varying the number of SILAR cycles.

In this work, the SILAR process was introduced to form the $ZnFe_2O_4/BiVO_4$ heterojunction by layer-by-layer deposition of $ZnFe_2O_4$ on $BiVO_4$ for the first time. Various characterizations about structural, morphological, and optical characterizations confirmed the formation of the $BiVO_4/ZnFe_2O_4$ heterojunction. Mott-Schottky and electrochemical impedance spectroscopy (EIS) analyses was also investigated to understand the nature of the heterojunction and charge transport properties in the heterojunction. The optimized $BiVO_4/ZnFe_2O_4$ heterojunction by control of SILAR process cycles showed enhanced PEC current and stability compared with the bare $BiVO_4$ in a neutral electrolyte. While the correlation among structural, morphological and optical properties is thoroughly discussed, the facile charge transport accounted for higher PEC performance. We provided the cost-effective and simple route to optimize $BiVO_4$ for the enhanced solar-driven water splitting.

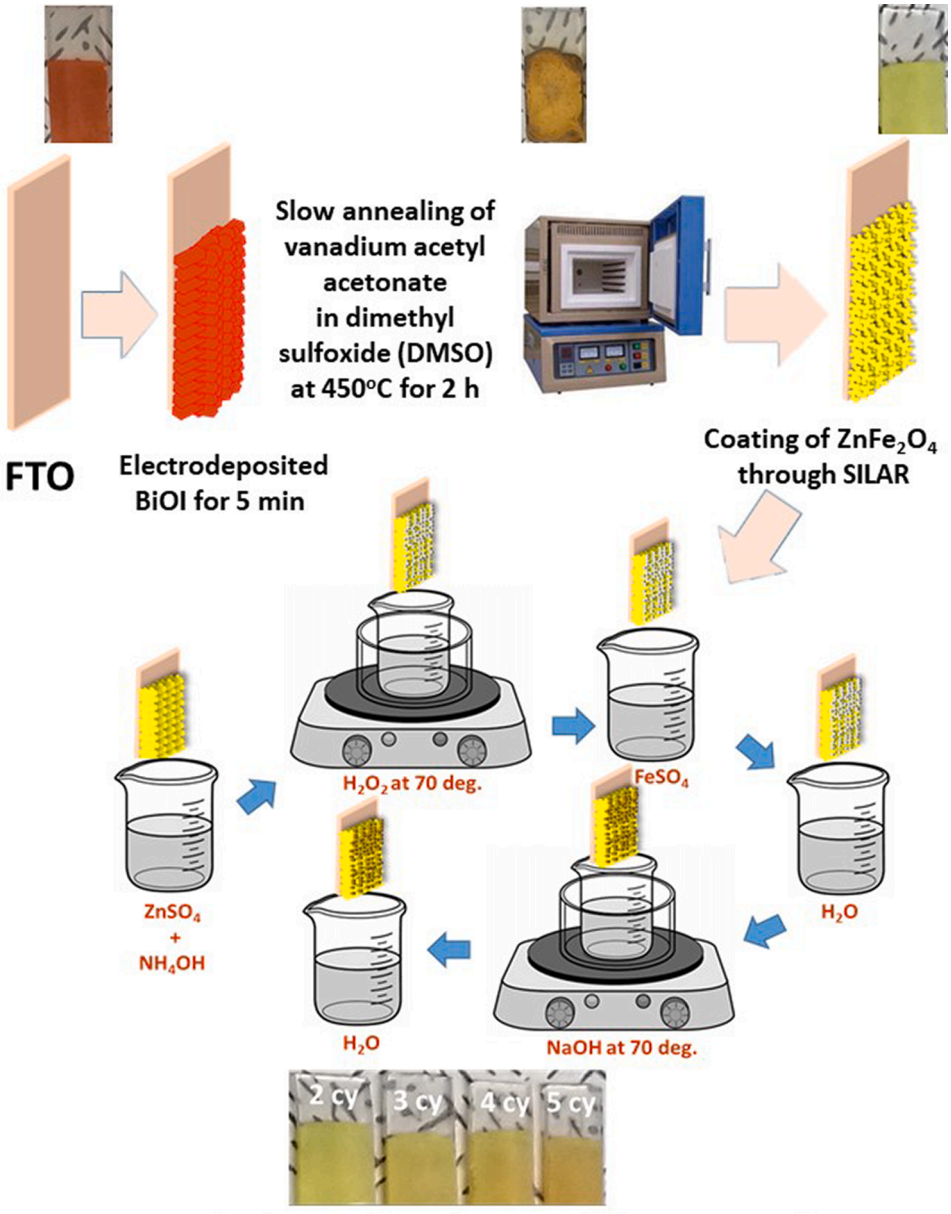

Fig. 1. Schematic flow for the complete fabrication process of $BiVO_4$ followed by the formation of the $ZnFe_2O_4$ over $BiVO_4$ nanostructured thin film.

2. Experimental

2.1. Materials

All of the chemicals used in this study were used as received. Bismuth (III) nitrate pentahydrate ($Bi(NO_3)_3{\cdot}5H_2O$), p-benzoquinone, dimethyl sulfoxide (DMSO), vanadyl acetyl acetonate, zinc sulfate heptahydrate ($ZnSO_4{\cdot}7H_2O$), iron (II) sulfate heptahydrate ($Fe_2SO_4{\cdot}7H_2O$), and sodium hydroxide (NaOH) were purchased from Sigma Aldrich. Hydrogen peroxide (H_2O_2) (purity: 34.5%) and potassium iodide (KI) were brought from Samchun, Korea. Lastly, ammonium hydroxide ($NH_4(OH)$), nitric acid (HNO_3) (purity: 60%) and sodium sulfate decahydrate ($Na_2SO_4{\cdot}10H_2O$) were obtained from Daejung and Junsei Korea, respectively.

2.2. Preparation of $BiVO_4$ nanostructure

For the fabrication of $BiVO_4$ nanostructure on the FTO-coated glass substrate (10 Ω/□), a simple two-step synthesis process was used as schematically described in Fig. 1. First, BiOI was grown by electrodeposition as reported previously [29]. Then, the conversion of BiOI to $BiVO_4$ was carried out by drop-casting of vanadyl acetyl acetonate in DMSO solution followed by slow annealing at 450 °C [30]. The details about experimental procedure are provided in the supplementary information (SI†).

2.3. Fabrication of $BiVO_4/ZnFe_2O_4$ electrodes

We modified the SILAR method reported by Raut *et al.* [31] to deposit $ZnFe_2O_4$ on $BiVO_4$ as shown in the schematic presented in Fig. 1. Briefly, in order to form $ZnFe_2O_4$ by SILAR, two cationic solutions, $ZnSO_4$ (0.025 M) and $FeSO_4$ (0.05 M), were used together with two anionic solutions, H_2O_2 (1%) and NaOH (0.01 M) aqueous solutions. During the formation of the precursor solution, the $ZnSO_4$ solution was complexed properly by a 30% liquid ammonia (NH_4OH) solution. Both anionic solutions were kept at 70 °C. For the proper deposition of $ZnFe_2O_4$ on the $BiVO_4$-coated FTO substrates, the substrates were immersed in a $ZnSO_4$ solution for 20 sec in order to adsorb Zn^{2+} ions and then dipped into the H_2O_2 solution for 15 sec to form $Zn(OH)_2$ complex. To adsorb Fe^{2+} on $Zn(OH)_2$, the substrates were immersed in a $FeSO_4$ solution for 20 sec, followed by the immersion of the substrates in the NaOH solution for another 15 sec. After this step, the conversion of Fe^{2+} to FeOOH occurred. Since the concentration of $FeSO_4$ was kept at twice than that of $ZnSO_4$, creating an additional adsorbed layer of Fe^{2+} on $Zn(OH)_2$, deionized water was placed before and after NaOH for proper rinsing. This rinsing step was carried out for 10 sec. The above procedure completes one SILAR cycle. The same process was repeated for 2, 3, 4 and 5 SILAR cycles. Finally, all of the substrates were kept at 300 °C to convert the hydroxide phases of Zn and Fe to $ZnFe_2O_4$ and also improve the crystallinity of the film.

2.4. Materials characterizations and PEC measurements

Structural analysis to confirm the crystalline nature of the bare $BiVO_4$ and the $ZnFe_2O_4$ coated on $BiVO_4$ was carried out using X-ray diffraction (XRD, Rigaku, D/MAX-RC) with Cu Kα radiation. The microstructures of films were examined by field emission scanning electron microscopy (FESEM, JSM700F, JEOL) and transmission electron microscopy (TEM, JEM-2100F HR, JEOL). Energy dispersive X-ray spectroscopy (EDS) coupled with TEM was used to probe the composition distribution of the samples. In addition, electronic structures of elements were studied by X-ray photoelectron spectroscopy (XPS, Kratos Axis Ultra DLD) with a monochromatic Al Kα X-ray source. The optical band gap energies for all of the samples were measured by UV–Visible spectroscopy (UV–Vis). Raman spectra were measured using a Uni-Ramspectrometer equipped with a laser at 532 nm. The PEC performance characteristics of the samples were investigated in dark and under the simulated sunlight condition (AM 1.5). Bare $BiVO_4$ or SILAR-coated $ZnFe_2O_4$ on $BiVO_4$ worked as the working electrodes (WE) while Ag/AgCl and Pt were used as the reference electrode (RE) and the counter electrode (CE), respectively. The electrolyte was a 0.5 M Na_2SO_4 aqueous solution with pH of 7.

3. Results and discussion

3.1. XRD characterization

Fig. 2(a) displays the XRD patterns of the bare $BiVO_4$ and $ZnFe_2O_4$ on $BiVO_4$ with 2, 3, 4 and 5 SILAR cycles (denoted by $BiVO_4/ZnFe_2O_4$ (2cy), $BiVO_4/ZnFe_2O_4$ (3cy), $BiVO_4/ZnFe_2O_4$ (4cy), and $BiVO_4/ZnFe_2O_4$ (5cy), respectively). The XRD pattern of the FTO substrate is shown together, of which peaks are marked with (#). The diffraction peaks match the scheelite monoclinic structure of $BiVO_4$ (JCPDS card no. 14–0688) [32]. No impurity phases were detected while peak ratios represent the polycrystalline phases of $BiVO_4$ without any preferential orientation during its growth on the FTO. It is clearly shown that the cubic spinel structure of $ZnFe_2O_4$ on $BiVO_4$ formed by the SILAR method. As SILAR cycles proceeded, the emergence of the diffraction peaks at ~ 37°, ~52°, and ~ 61° corresponding to (311), (422), and (440) lattice planes of $ZnFe_2O_4$ (JCPDS card no. 22–1012) could be

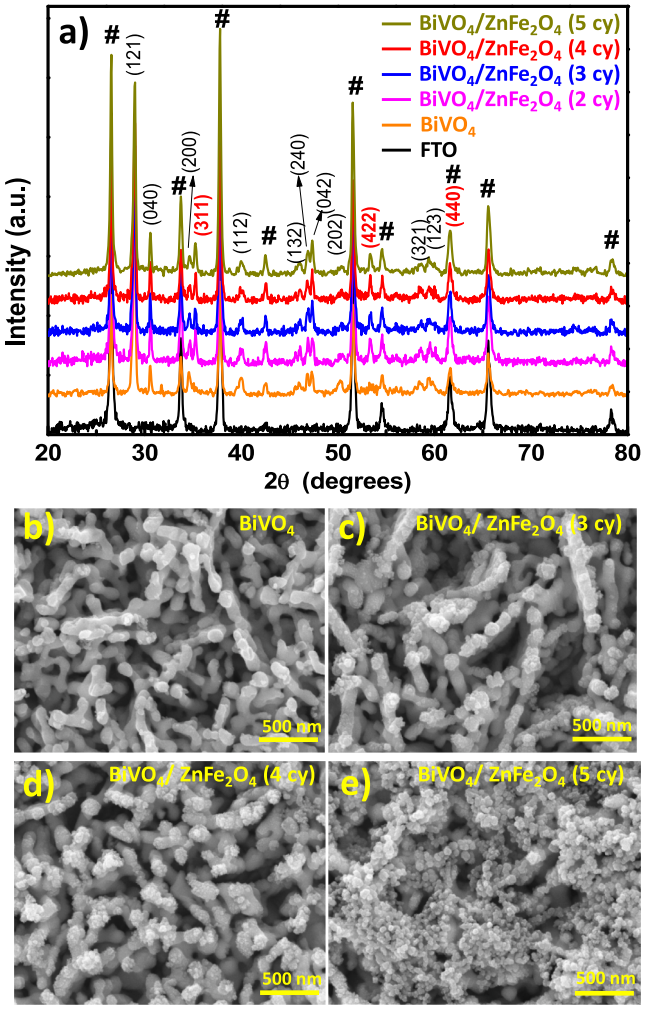

Fig. 2. (a) XRD patterns of the bare $BiVO_4$ and SILAR-coated $ZnFe_2O_4$ over $BiVO_4$ with the different number of SILAR cycles. FESEM images present the (b) bare $BiVO_4$ and those coated by $ZnFe_2O_4$ with (c) three, (d) four, and (e) five SILAR cycles.

observed. Further for better comparison we have perform the XRD for only $ZnFe_2O_4$ deposited by the 4 cy SILAR over glass followed by annealing for 300 °C which is shown as the Figure S1†. XRD peaks confirm the formation of $BiVO_4$ and $ZnFe_2O_4$ without any undesired phases during the chemical synthesis.

3.2. SEM and TEM analysis

FESEM images of the bare $BiVO_4$ and $ZnFe_2O_4$-deposited $BiVO_4$ with different numbers of SILAR cycles are shown in Fig. 2(b)-(e). The $BiVO_4$ nanorods were quasi-vertically grown on the FTO substrate as shown in Fig. 2(b). The $BiVO_4/ZnFe_2O_4$ (3cy), $BiVO_4/ZnFe_2O_4$ (4cy), and $BiVO_4/ZnFe_2O_4$ (5cy), respectively, are presented in Fig. 2(c), (d), and (e). The growth of the $ZnFe_2O_4$ could be observed by gradual increase in coverage of $ZnFe_2O_4$ on $BiVO_4$ up to four SILAR cycles. Meanwhile, overgrowth of $ZnFe_2O_4$ on $BiVO_4$ nanostructure occurred at the fifth SILAR cycle. At the fifth SILAR cycle, growth of $ZnFe_2O_4$ occurred not only at the surface of the $BiVO_4$ structure but also at the pre-grown $ZnFe_2O_4$ nanoparticles (Fig. 2(e)).

The TEM analysis about the $BiVO_4/ZnFe_2O_4$ (4cy) is carried out in Fig. 3(a). $ZnFe_2O_4$ covered the whole surface of $BiVO_4$ as confirmed by EDS mapping. Fig. 3(b), (c), (d), (e), and (f) correspond EDS elemental mappings for Bi, V, O, Zn, and Fe, respectively, revealing homogeneous distribution of each element throughout the structure. The morphology of the $BiVO_4/ZnFe_2O_4$ (4cy) could be studied by High-resolution TEM (HRTEM) in detail. Fig. 3(g) and 3(h) display the HRTEM images of the region as marked by the red square region 1 and 2 in Fig. 3(a), respectively. Interestingly, while conformal deposition of amorphous $ZnFe_2O_4$ could be achieved on the surface of $BiVO_4$ as shown in the Fig. 3(h), $ZnFe_2O_4$ nanocrystals of nanoparticles with lattice planes corresponding to (3 1 1) and (4 4 0) planes also could be observed on the outer surface (Fig. 3(g)). It seems that $ZnFe_2O_4$ was preferentially grown on the surface of $BiVO_4$ at the initial stage. Then, once the full coverage of $ZnFe_2O_4$ is achieved, crystallization of $ZnFe_2O_4$ occurs. The selected area electron diffraction (SAED) pattern in the inset shows the coexistence of crystalline and amorphous phases. Our studies about the microstructure confirmed the formation of the heterojunction between $BiVO_4$ and $ZnFe_2O_4$ as well as nucleation and growth behavior of $ZnFe_2O_4$.

3.3. XPS analysis

X-ray photoelectron spectroscopy (XPS) survey scans of the bare $BiVO_4$ and $BiVO_4$/ $ZnFe_2O_4$(4 cy), Fig. 4(a), showed the presence of the constituent elements such as Zn, Fe, Bi, V, and O. Fig. 4(b), (c), (d), (e), and (f) present the high-resolution spectrum of Zn 2*p*, Fe 2*p*, Bi 4*f*, V 2*p*, and O 1 *s*, respectively. Fig. 4(b) exhibits the peaks at the binding

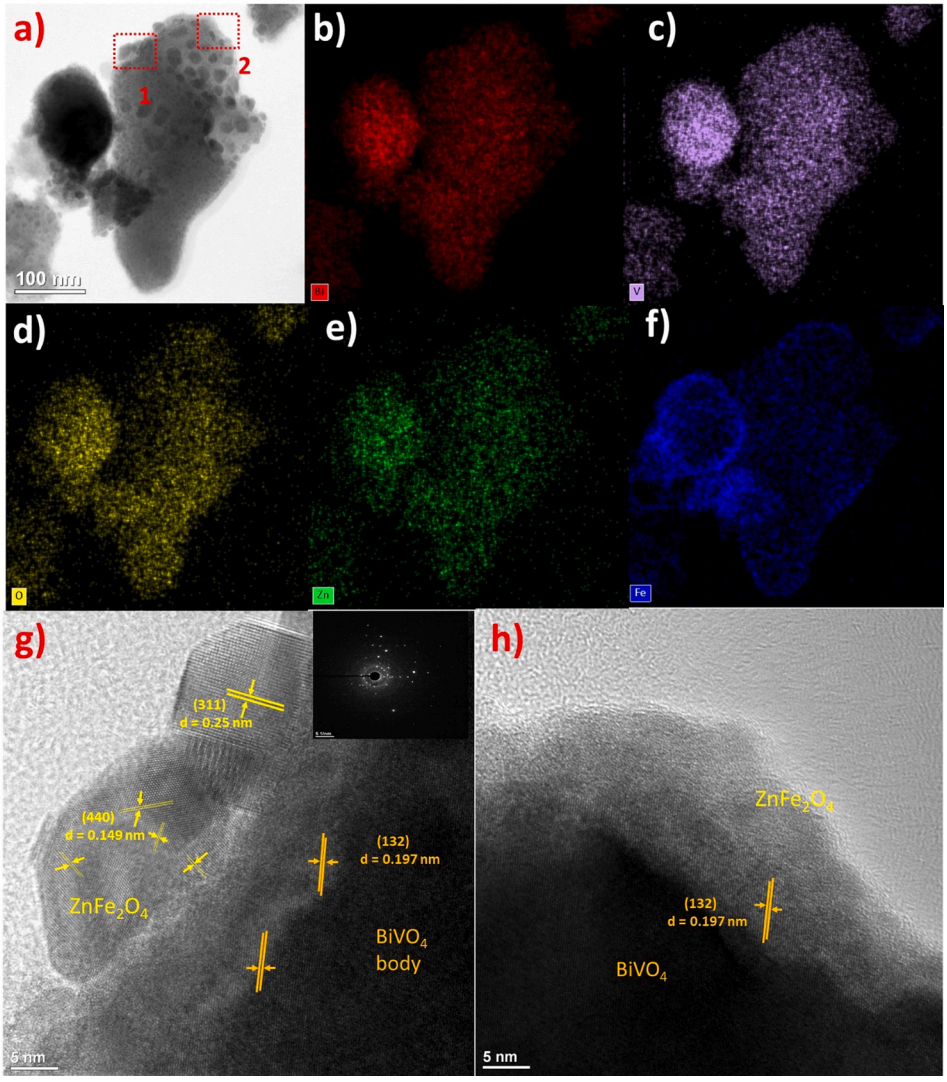

Fig. 3. (a) TEM image of $BiVO_4$/ $ZnFe_2O_4$ (4 cy) with the EDS mapping of (b) Bi, (c) V, (d) O, (e) Zn, and (f) Fe. (g) HR-TEM image of the region 1 of (a) $BiVO_4$/ $ZnFe_2O_4$ (4 cy) with an inset of the SAED pattern whereas (h) shows HR-TEM image of the region 2 highlighted in (a).

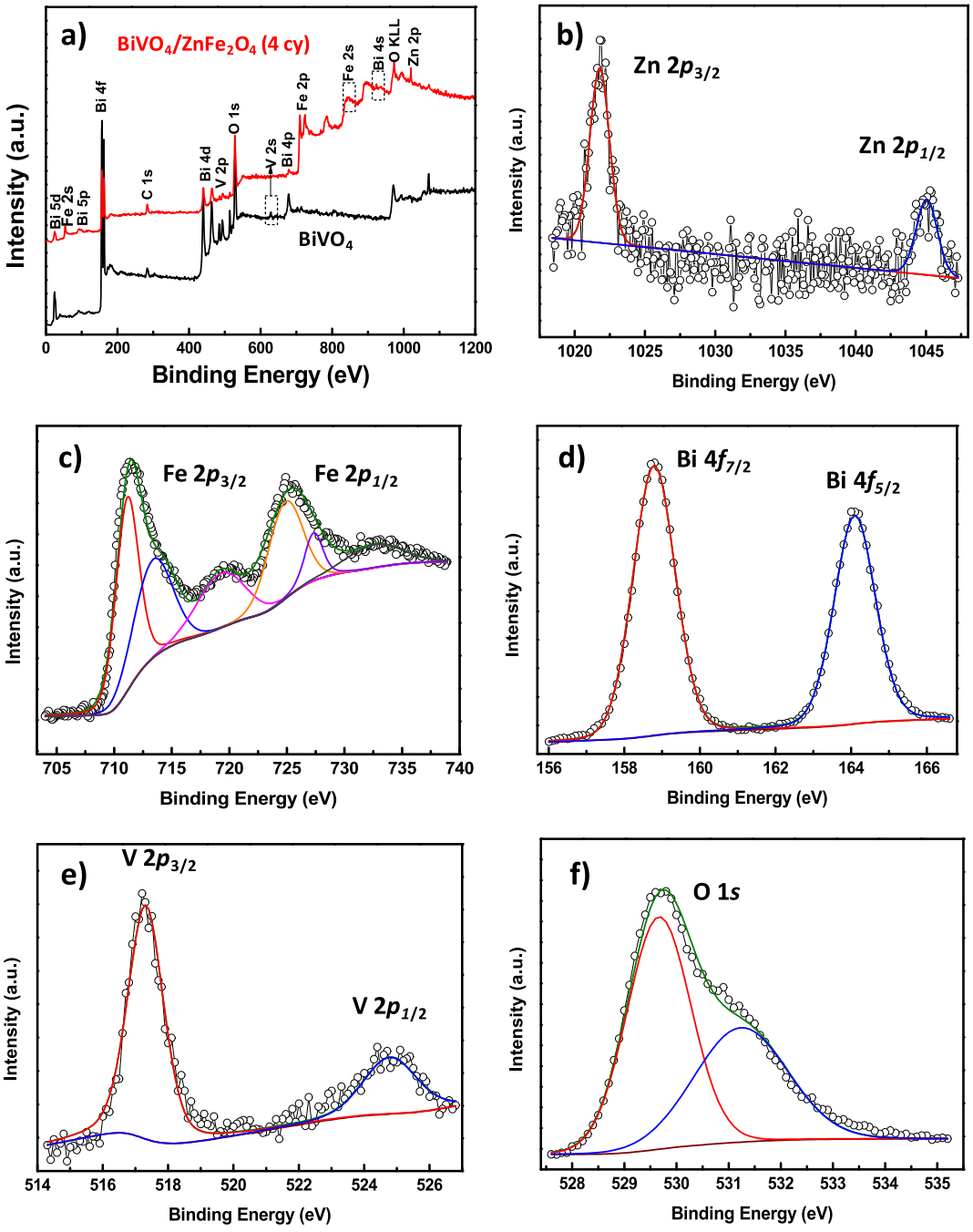

Fig. 4. XPS survey scans of bare $BiVO_4$ and $BiVO_4/ZnFe_2O_4$ (4 cy). XPS fine scans of $BiVO_4/ZnFe_2O_4$ (4 cy) for the core electron level spectra of (b) Zn, (c) Fe, (d) Bi, (e) V, and (f) O.

energies (B.E.) of 1021.8 and 1045 eV corresponding to Zn $2p_{3/2}$ and Zn $2p_{1/2}$ states, respectively, of which energies are consistent with Zn^{2+} oxidation state [33]. Peaks at 711.8 and 725.4 eV in Fe 2*p* spectra Fig. 4 (c) are attributed to Fe $2p_{3/2}$ and Fe $2p_{1/2}$, respectively [34]. The deconvolution of Fe 2*p* showed mixed state of Fe^{2+} and Fe^{3+} [35]. In the normal spinel structure, Fe^{3+} resides on the octahedral site, however, site mixing with Zn^{2+} in the tetrahedral site can lead to the mixed oxidation state of Fe [36].The deconvoluted peaks at 711.8 and 725.4 eV in Fe 2p spectra could shows the state of Fe^{3+} [37]. Mixed state of Fe^{3+} and Fe^{2+} ions in the spinel structure induces the off stoichiometry such as oxygen vacancy, therefore revealing n-type behavior [38,39]. XPS fine scans of Bi and V, Fig. 4(d) and (e), show Bi $4f_{7/2}$ and Bi $4f_{5/2}$, and V $2p_{3/2}$ and V $2p_{1/2}$, respectively, in $BiVO_4$, where Bi^{3+} and V^{+5} exist in the crystalline structure [40]. Meanwhile, Fig. 4(f) presents asymmetric O 1*s* spectra that were deconvoluted into two sub peaks. The peak at ~ 529.6 eV confirms that the oxygen is found to exist as −2 state in the metal oxide, whereas the peak at ~ 531.2 eV is associated with the presence of adsorbed water at the surface [41,42].

3.4. Raman analysis

Raman spectra of the bare $BiVO_4$ and $ZnFe_2O_4/BiVO_4$ with different SILAR cycles are investigated as shown in Fig. 5(a). In the bare $BiVO_4$, the characteristics Raman bands at ~ 824 and ~ 711 cm^{-1} are corresponding to the symmetric (υ_s) and asymmetric deformation modes (υ_{as}) of the (V-O) bond, respectively. Here, υ_s dominates as described by Peng *et al.*,[43] confirming the monoclinic structure of $BiVO_4$. The peaks at ~ 362 and ~ 326 cm^{-1} suggests the formation of the bending mode of

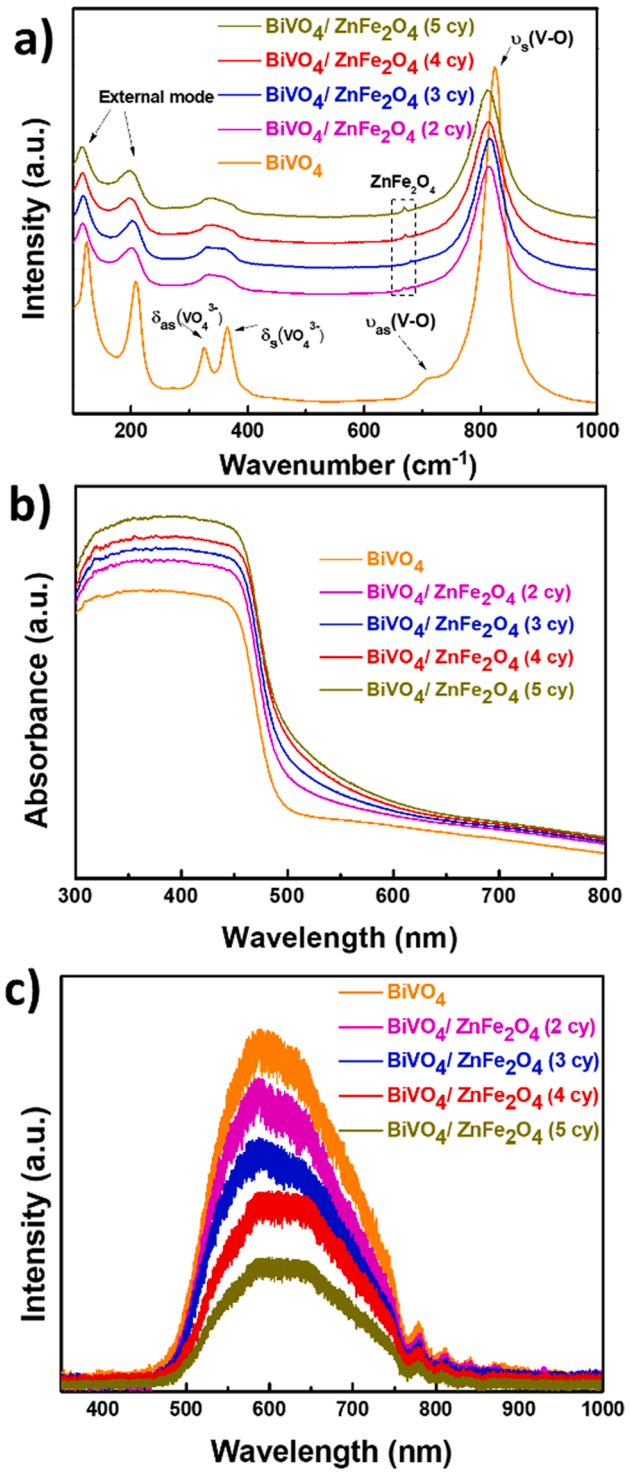

Fig. 5. (a) Raman spectra, (b) UV–Visible spectra, and (c) photoluminescence spectra of $BiVO_4$ and $BiVO_4/ZnFe_2O_4$ with different SILAR cycles.

(A_{1g}) both symmetric and antisymmetric deformations of vanadate ion (VO_4^{3-}) [43,44]. Features at ~ 207 and ~ 126 cm^{-1} are assigned to the rotational and translation behaviors of the external modes in $BiVO_4$, respectively [37]. As the $ZnFe_2O_4$ was deposited on the $BiVO_4$ surface through the SILAR cycles, interesting changes in the Raman spectra could be observed. The emergence of peaks at approximately 683 cm^{-1} and 344 cm^{-1} resulted from the A_{1g} and F_{2g} mode, respectively, from the cubic spinel $ZnFe_2O_4$ structure [45]. The blue shift of Raman spectra compared with pure $ZnFe_2O_4$ was observed, which can result from the compressive stress by the heterojunction between $ZnFe_2O_4$ and $BiVO_4$ [46,47]. It should be noted that red shift of the υ_s in V-O bonding in $BiVO_4$ occurred simultaneously, which could be originated from the tensile stress applied to $BiVO_4$ [48,49]. Such systematic changes in the Raman further support successful formation of the $BiVO_4/ZnFe_2O_4$ heterojunction. Meanwhile, both υ_{as} and υ_{as} of the V-O bonding in $BiVO_4$ showed sharp decrease by the increase of SILAR cycle possibly due to the surface sensitivity of Raman spectra.

3.5. Optical and photoluminescence studies

The absorption spectra for bare and $ZnFe_2O_4$-coated $BiVO_4$, Fig. 5(b), show the increase of intensity and broadening of spectra in the wavelength range of 440–700 nm as the increase of the SILAR cycle. Such increase of intensity and broadening to the large wavelength can be attributed to the formation of $ZnFe_2O_4$ on $BiVO_4$, which becomes more prominent by the increase in the volume of $ZnFe_2O_4$ as more SILAR cycles proceed. Gradual increase of absorbance and broadening of spectra can result from the increase of $ZnFe_2O_4$ and simultaneous formation of $BiVO_4/ZnFe_2O_4$ heterojunction with a smaller bandgap compared with bare $BiVO_4$. The optical band gap could be estimated using the Tauc's formula. Fig. S2† shows the optical band gap of 2.56 eV for the bare $BiVO_4$, which is consistent with the earlier report [8,50]. Meanwhile, optical band gaps can be estimated to be 2.55, 2.54, 2.52, and 2.50 eV for $BiVO_4/ZnFe_2O_4$ (2cy), $BiVO_4/ZnFe_2O_4$ (3cy), $BiVO_4/ZnFe_2O_4$ (4cy), and $BiVO_4/ZnFe_2O_4$ (5cy), respectively. $ZnFe_2O_4$ with the small band gap (~1.90 eV) on the surface resulted in the decrease in the band gap of the $BiVO_4/ZnFe_2O_4$ nanostructure [51]. The steady-state room temperature photoluminescence (PL) spectra of all samples excited at the wavelength of 325 nm are shown in Fig. 5(c). It is reported that the strong single emission could be observed at ~ 560 nm, which is attributed to the recombination of the holes in the hybrid orbital states of Bi 6 *s* and O 2*p*, and the electrons at the V3*d* orbital [52,53]. On the other hand, as shown in Fig. 5(c), the broad PL emission was observed between 500 and 750 nm, which can result from the defect levels in the hydrothermally synthesized $BiVO_4$ [54]. The increase in the number of SILAR cycles for $ZnFe_2O_4$ resulted in a sharp decrease in the PL emission. Many factors such as thickness, defects, size, etc. can affect such decease in the PL emission [55]. However, considering the very small volume of $ZnFe_2O_4$ compared with $BiVO_4$, higher separation between holes and electrons followed by lower recombination, so called PL quenching, can be most responsible to such decrease of PL emission,[56] which will be discussed in detail later.

3.6. Photoelectrochemical performance

Linear sweep voltammetry (LSV) was employed to obtain the current density- voltage (J-V) curves in dark or under the light as shown in Fig. 6 (a). All samples showed negligible current in dark, however, the current increased significantly by light radiation due to the PEC effect. The significant increase in the PEC current density could be observed as the increase in the number of the SILAR cycles up to 4 cycles. The bare $BiVO_4$ showed only 0.73 mA/cm^2, however, 0.99, 1.15, and 1.44 mA/cm^2 could be attained in the $BiVO_4/ZnFe_2O_4$ (2cy), $BiVO_4/ZnFe_2O_4$ (3cy), and $BiVO_4/ZnFe_2O_4$ (4cy), respectively. In the meantime, $BiVO_4/ZnFe_2O_4$ (5cy) revealed rather decreased current density of 1.28 mA/cm^2. Though it is not clear about the origin of decrease in PEC performance for the 5 SILAR cycle, the morphology in Fig. 3(g) of the aggregated $ZnFe_2O_4$ particles suggests that the photo-carriers generated in each particle can reveal low transport to the electrode while hindering the contact of the electrolyte with the regular $BiVO_4/ZnFe_2O_4$ junction. This will reduce the effective surface area of the electrode in the contact with the electrolyte as well as hinder the facile permeation of electrolyte to the whole electrode structure, particularly near the FTO side.

Transient PEC current plots were obtained at 1 V vs SCE to investigate the photoelectrochemical stability as shown in Fig. 6(b). The PEC

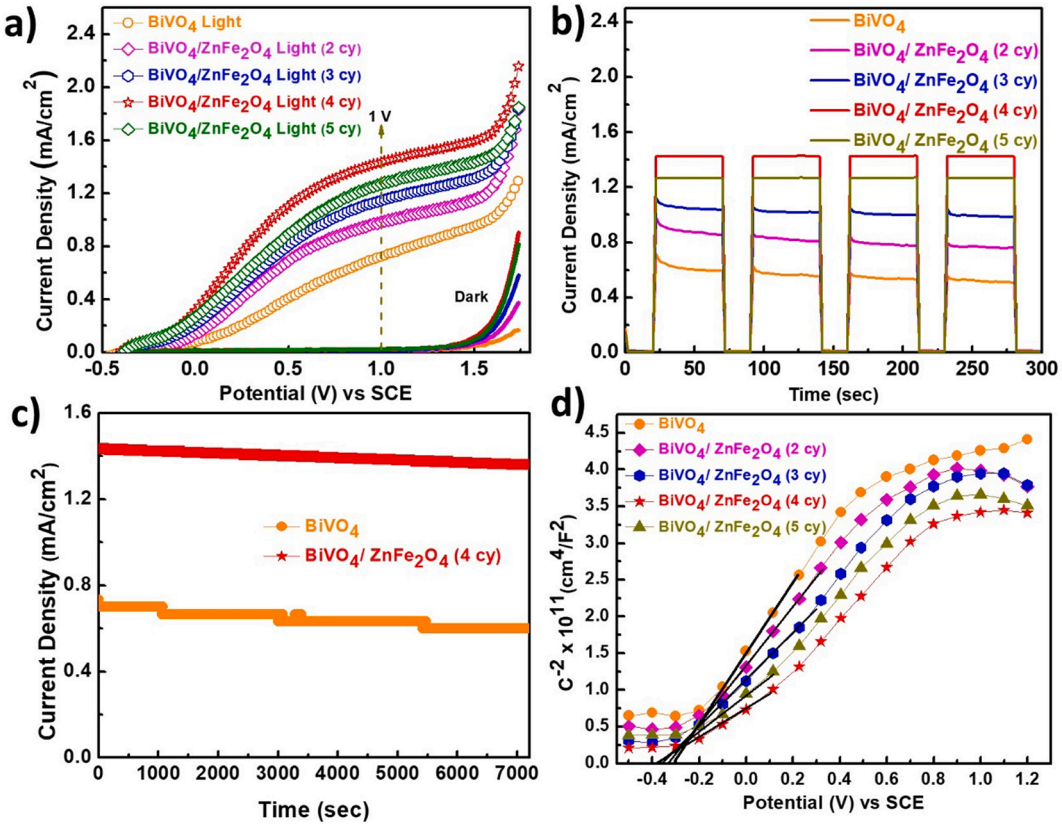

Fig. 6. Current density vs. Voltage curves of the bare $BiVO_4$ and $BiVO_4/ZnFe_2O_4$ photoanodes with the scan rate of 10 mV/s in the potential range between −0.5 and 1.7 V (vs SCE). (b) Transient PEC current densities of the electrodes at 1 V vs SCE in 0.5 M of Na_2SO_4 neutral electrolyte during extended cycles with and without illumination. (c) Chronoamperometric measurement at 1 V vs SCE for the bare $BiVO_4$ and $BiVO_4/ZnFe_2O_4$ (4cy) photoanodes under simulated light. (d) The Mott-Schottky plot of the photoanodes derived from J-V curves.

current density changed rapidly by the illumination, showing the response kinetics of the electrodes. Compared to the gradual decrease in PEC current for bare $BiVO_4$, $BiVO_4$/ $ZnFe_2O_4$ (2cy), and $BiVO_4$/ $ZnFe_2O_4$ (3cy) electrodes, it should be noted that the $BiVO_4$/ $ZnFe_2O_4$ (4cy) and $BiVO_4$/ $ZnFe_2O_4$ (5cy) showed very stable PEC current densities even during the extended cycles. This observation indicates that the complete coverage or the threshold thickness of $ZnFe_2O_4$ is required to obtain the PEC stability of $BiVO_4$. To further investigate the PEC stability, the chronoamperometric measurement, Fig. 6(c), was carried out for bare $BiVO_4$ and $ZnFe_2O_4/BiVO_4$ (4cy) electrodes under the AM1.5 light condition for 2 h. The comparison manifests the effect of $ZnFe_2O_4$ based heterojunction on the PEC stability of the $BiVO_4$ electrode. The bare $BiVO_4$ showed 81% of PEC current retention after the oxidation for 2 hr. On the other hand, the $BiVO_4/ZnFe_2O_4$ (4cy) heterojunction showed 94% of PEC current retention.

The Mott-Schottky plot derived from the J-V curves of bare $BiVO_4$ and $BiVO_4/ZnFe_2O_4$ electrodes is shown in Fig. 6(d). The positive slopes of the curves in the Mott-Schottky plot prove an n-type semiconducting behavior of the $BiVO_4$ electrodes regardless of heterojunction with $ZnFe_2O_4$ [57]. The flat-band potentials (V_{fb}) were calculated from the extrapolation of C^{-2} to the potential axis [58]. The flat-band potentials slightly shifted to the more negative potential as the thicker $ZnFe_2O_4$ formed on the heterojunction Table 1. Since the measurement reveals the estimation of V_{fb} in the electrodes, the $BiVO_4$-based heterojunction structure with the thicker $ZnFe_2O_4$ results in the higher band bending at the electrode/electrolyte interface, which ultimately leads to the more efficient charge separation at the junction followed by the enhanced PEC current density [59]. Furthermore, the slope, C^{-2} over V, varies with the

Table 1
Relevant parameters of bare $BiVO_4$ and $BiVO_4$ $ZnFe_2O_4$ heterojunction with different numbers of SILAR cycle.

Sl. No.	Label	J_{sc} at 1 V (vs SCE) (mA/cm^2)	V_{fb} (V vs SCE)	R_s (Ω)	R_{ct} (Ω)	C (μF)	τ_e (ms)	k_{eff} (s^{-1})
1.	$BiVO_4$	0.73	−0.30	33.80	3538	8.133	30.18	33.12
2.	$BiVO_4$/ $ZnFe_2O_4$(2 cy)	0.99	−0.33	33.46	2944	9.209	30.85	32.40
3.	$BiVO_4$/ $ZnFe_2O_4$(3 cy)	1.15	−0.34	32.81	2275	14.34	31.55	31.69
4.	$BiVO_4$/ $ZnFe_2O_4$(4 cy)	1.44	−0.36	32.64	1314	33.96	34.21	29.22
5.	$BiVO_4$/ $ZnFe_2O_4$(5 cy)	1.28	−0.36	32.75	1507	22.37	32.36	30.89

potential for the heterojunction electrodes. The slope at 0.5 V is higher than that at 0 V. Considering the capacitance–voltage measurement theory in the semiconductor, the dopant concentration of $BiVO_4$ is lower than that of $ZnFe_2O_4$ as indicated by higher and lower slope at 0.5 V and 0 V, respectively.

The charge transport characteristics of the electrodes were also studied by the electrochemical impedance spectroscopy (EIS), Fig. 7. The Nyquist plots of the bare $BiVO_4$ and $BiVO_4/ZnFe_2O_4$ photoanodes, Fig. 7(a), were recorded at 1 V vs. SCE in a 0.5 M Na_2SO_4 aqueous solution. The bias condition was same with that in transient PEC current or chronoamperometric measurement, which can extend the depletion depth far into the $BiVO_4$ layer through the $ZnFe_2O_4$ layer. The simple equivalent circuit shown in the inset of the Fig. 7(a) was used to fit the EIS data. The particular Randles model for this AC response is commonly used for the $BiVO_4$-based heterojunctions as described by Hegner *et al.* [60,61] R_s derived from series connection of the FTO substrate and the FTO/$BiVO_4$ junction is relatively small and rather constant regardless of the $ZnFe_2O_4$ layer thickness. Therefore, R_s values of all electrodes are similar as can be seen in Table 1. Whereas, R_{ct} and C represent the junction built in at the contact with the electrolyte under the given bias. The bare $BiVO_4$ showed the highest R_{ct} and the smallest C among the electrodes due to the lower doping in the $BiVO_4$ than that in $ZnFe_2O_4$ as discussed in the Mott-Schottky plot, Fig. 6(d). On the other hand, the R_{ct} and C measured at the positive potential (1 V vs. SCE) for the $BiVO_4$/$ZnFe_2O_4$ heterojunctions are the resistance and capacitance of the serial connection of $ZnFe_2O_4$ and $BiVO_4$ layer under carrier depletion.

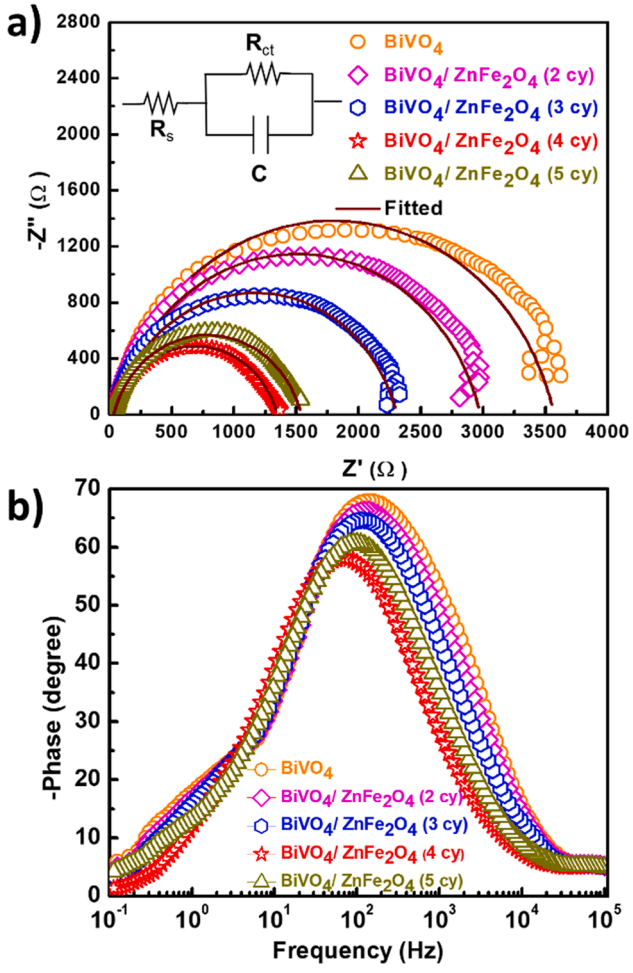

Fig. 7. (a) The Nyquist and (b) Bode phase plot of the different electrodes at 1 V vs SCE in the 0.5 M of Na_2SO_4 electrolyte with the inset showing the equivalent circuit diagram.

The electrical measurements of the Mott-Schottky and EIS can be understood based on energy band diagram in Fig. 8. Fig. 8(a) schematically illustrates the band alignment for type II heterojunction of undoped intrinsic $BiVO_4/ZnFe_2O_4$. The conduction band and valence band positions of $ZnFe_2O_4$ are relatively more negative than those of $BiVO_4$ on the NHE scale. However, both $BiVO_4$ and $ZnFe_2O_4$ are n-type doped, thus they reveal the positive band bending (eV_b) at the semiconductor/electrolyte contact, of which equilibrium condition at the semiconductor/electrolyte contact is illustrated in Fig. 8(b). Since $ZnFe_2O_4$ is more highly n-type doped compared with $BiVO_4$, the higher band bending at the interface between $ZnFe_2O_4$ and the electrolyte could be observed. Because the depletion depth, d, at the semiconductor/electrolyte junction is the function of (V_b) and doping (or the Fermi level E_F), the depletion junction depth of $ZnFe_2O_4$ is shrunk and extended with a higher dopant concentration and band bending, respectively, compared to $BiVO_4$. Considering the uncertainty about doping concentration, the scale of depletion depth shown in Fig. 8 is arbitrary, however, this does not influence the qualitative discussion as follows.

When $ZnFe_2O_4$ begins to be deposited on $BiVO_4$ by the SILAR process, islands of amorphous $ZnFe_2O_4$ seem to nucleate and grow rather than a layer-by-layer growth as indicated by the HRTEM analysis. The band diagram of the junction through the $ZnFe_2O_4$ island can be drawn like Fig. 8(c) for $BiVO_4/ZnFe_2O_4$ heterojunction in contact with the electrolyte. However, the $BiVO_4$ nanorod surface is not uniformly covered with $ZnFe_2O_4$, and parts of the surface directly contact with the electrolyte. The incomplete coverage of $ZnFe_2O_4$ on the $BiVO_4$ nanorod could result in the photocurrent degradation during the extended PEC measurement for the samples with less than three SILAR cycles as shown in Fig. 6(b). However, after four SILAR cycles, the whole $BiVO_4$ nanorod surface could be deposited by $ZnFe_2O_4$ accompanied by the partial crystallization of $ZnFe_2O_4$. The band diagram will develop towards Fig. 8(d) as the further SILAR deposition proceeds. Therefore, the capacitance C measured at a reverse bias of 1 V (vs SCE) is originated from the series-connected depletion junction capacitances of $ZnFe_2O_4$ and $BiVO_4$. The higher C with increasing SILAR cycles indicates decreasing depletion depth due to the semiconductor junction theory, $C = A\varepsilon/d$, where A, ε, and d are the surface area, dielectric permittivity of the material, and the depletion junction depth, respectively. The change of the depletion depth matches the equilibrium condition established in Fig. 8(b), i.e., smaller depletion depth with $ZnFe_2O_4$ than $BiVO_4$. Therefore, the higher photocurrent observed with $BiVO_4$/$ZnFe_2O_4$ (4cy) heterojunction was ascribed to the higher band bending or higher built-in electric field at the $BiVO_4/ZnFe_2O_4$/electrolyte junction, which enhanced electron-hole separation minimizing their recombination.

The $BiVO_4/ZnFe_2O_4$ (4cy) heterojunction shows lowest R_{ct} and largest C, therefore the best PEC performance could be achieved, and in which higher band bending could occur. In the meantime, slight increase of R_{ct} accompanied by decrease of C was observed in the $BiVO_4$/$ZnFe_2O_4$ (5cy) heterojunction compared with $BiVO_4/ZnFe_2O_4$ (4cy), which resulted from the loss of the active surface area by $ZnFe_2O_4$ agglomeration, which does not form a successful heterojunction with the underlying $BiVO_4$. The combination of increased R_{ct} and decreased C could account for the increase in total impedance in the $BiVO_4/ZnFe_2O_4$ (5cy). All in all, the EIS analysis about the electrodes clearly agrees with the PEC performance. Fig. 8(b) shows the Bode plot of the electrodes that is derived from EIS. It is clear that shift of the peak in phase angle toward lowest frequency with decrease in the angle occurs by the formation of heterojunction with $ZnFe_2O_4$. The Bode plot exhibits the charge transport time factor, τ_n ($= 1/2\pi f_m$), where (f_m) is the characteristic frequency [62,63]. As summarized in Table 1 and Fig. 8(b), for the $BiVO_4/ZnFe_2O_4$ (4cy), the charge transport time factor showed the maximum, thus the rate of recombination (k_{eff}) that is inversely proportional to τ_n is minimum. Therefore, the $BiVO_4/ZnFe_2O_4$ heterojunction reveals enhancement in the PEC performance compared to the

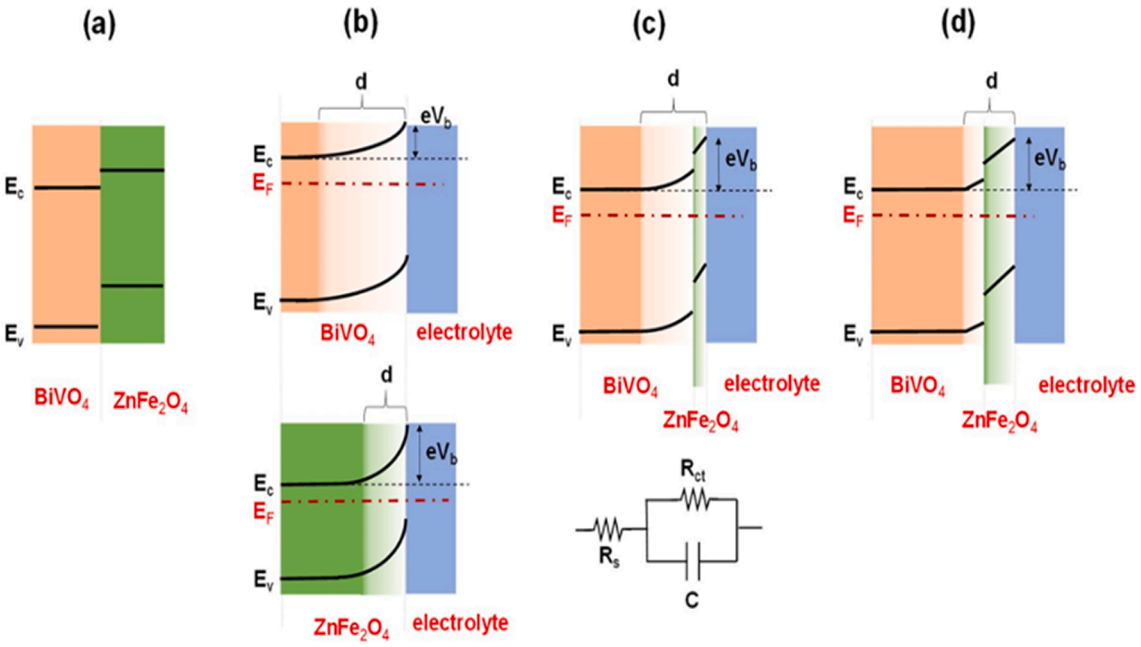

Fig. 8. (a) The schematic of the type II intrinsic $BiVO_4/ZnFe_2O_4$ heterojunction. (b) The semiconductor/electrolyte junction showing the built-in potential eV_b (band bending) and depletion depth, *d*, in the semiconductor following the Mott-Schottky measurements. The $BiVO_4/ZnFe_2O_4$/electrolyte junction with the relatively (c) thin and (d) thick $ZnFe_2O_4$ surface layer. The equivalent circuit used for the fitting of EIS measurements is also shown. With higher-doping $ZnFe_2O_4$, the depletion junction depth decreases while leading to higher C.

bare $BiVO_4$ with high rate of recombination of charges.

4. Conclusions

In conclusion, the $BiVO_4/ZnFe_2O_4$ heterojunction was developed through the low-cost SILAR method. The successful formation of the heterojunction between $BiVO_4$ and $ZnFe_2O_4$ was confirmed by various analytical tools. The optimized $BiVO_4/ZnFe_2O_4$ heterojunction with the proper thickness of $ZnFe_2O_4$ revealed the enhanced PEC current and stability compared with the bare $BiVO_4$. While the bare $BiVO_4$ photoanode showed the short life time for photocarriers, the $BiVO_4/ZnFe_2O_4$ heterojunction revealed the facile charge transport properties owing to higher band bending at the interface with the electrolyte followed by the extended charge life time. We believe the SILAR process to architect the high quality heterojunction on the surface can provide new opportunities for the fabrication of highly efficient photoanodes for PEC water splitting.

CRediT authorship contribution statement

Sutripto Majumder: Conceptualization, Methodology, Formal analysis, Data curation, Validation, Writing - original draft, Writing - review & editing. **Nguyen Duc Quang:** Formal analysis, Data curation. **Truong Thi Hien:** Formal analysis. **Nguyen Duc Chinh:** Formal analysis. **Nguyen Manh Hung:** Formal analysis. **Haneul Yang:** Formal analysis. **Chunjoong Kim:** Validation, Formal analysis. **Dojin Kim:** Supervision, Resources.

Declaration of Competing Interest

The authors declare that they have no known competing financial interests or personal relationships that could have appeared to influence the work reported in this paper.

Acknowledgment

This work was supported by the National Research Lab program (2018R1A2A1A 05023126) of the National Research Foundation of Korea.

Appendix A. Supplementary data

Supplementary data to this article can be found online at https://doi.org/10.1016/j.apsusc.2021.149033.

References

[1] S. Cho, J.-W. Jang, K.-H. Lee, J.S. Lee, APL Mater. 2 (2014), 010703.
[2] A. Fujishima, K. Honda, Nature 238 (1972) 37.
[3] C. Santato, M. Ulmann, J. Augustynski, J. Phys. Chem. B 105 (2001) 936–940.
[4] A. Kay, I. Cesar, M. Grätzel, J. Am. Chem. Soc. 128 (2006) 15714–15721.
[5] Y. Li, Z. Liu, Y. Wang, Z. Liu, J. Han, J. Ya, Int. J. Hydrogen Energy 37 (2012) 15029–15037.
[6] K. He, J. Xie, M. Li, X. Li, Appl. Surf. Sci. 430 (2018) 208–217.
[7] J. Cen, Q. Wu, D. Yan, J. Tao, K. Kisslinger, M. Liu, A. Orlov, PCCP 19 (2017) 2760–2767.
[8] K. Sayama, A. Nomura, T. Arai, T. Sugita, R. Abe, M. Yanagida, T. Oi, Y. Iwasaki, Y. Abe, H. Sugihara, J. Phys. Chem. B 110 (2006) 11352–11360.
[9] K. Okuno, H. Kato, J.Jhon M. Vequizo, A. Yamakata, H. Kobayashi, M. Kobayashi, M. Kakihana, RSC Advances, 8 (2018) 38140-38145.
[10] L. Wang, J. Liu, W. Song, H. Wang, Y. Li, J. Liu, Z. Zhao, J. Tan, Z. Duan, J. Deng, Chem. Eng. J. (2019).
[11] Y. Park, K.J. McDonald, K.-S. Choi, Chem. Soc. Rev. 42 (2013) 2321–2337.
[12] B.J. Trześniewski, W.A. Smith, J. Mater. Chem. A 4 (2016) 2919–2926.
[13] J.-S. Yang, J.-J. Wu, Nano Energy 32 (2017) 232–240.
[14] S.P. Berglund, A.J.E. Rettie, S. Hoang, C.B. Mullins, PCCP 14 (2012) 7065–7075.
[15] R. Saito, Y. Miseki, K. Sayama, Chem. Commun. 48 (2012) 3833–3835.
[16] S.K. Pilli, T.E. Furtak, L.D. Brown, T.G. Deutsch, J.A. Turner, A.M. Herring, Energy Environ. Sci. 4 (2011) 5028–5034.
[17] S.J.A. Moniz, S.A. Shevlin, D.J. Martin, Z.-X. Guo, J. Tang, Energy Environ. Sci. 8 (2015) 731–759.
[18] L. Xia, J. Bai, J. Li, Q. Zeng, L. Li, B. Zhou, Appl. Catal. B 204 (2017) 127–133.
[19] D. Lee, A. Kvit, K.-S. Choi, Chem. Mater. 30 (2018) 4704–4712.
[20] S.-Y. Chen, J.-S. Yang, J.-J. Wu, ACS Appl. Energy Materials 1 (2018) 2143–2149.
[21] M.N. Shaddad, D. Cardenas-Morcoso, P. Arunachalam, M. García-Tecedor, M. A. Ghanem, J. Bisquert, A. Al-Mayouf, S. Gimenez, J. Phys. Chemistry C 122 (2018) 11608–11615.
[22] T.-G. Vo, J.-M. Chiu, Y. Tai, C.-Y. Chiang, Sol. Energy Mater. Sol. Cells 185 (2018) 415–424.
[23] Y. Hou, X.-Y. Li, Q.-D. Zhao, X. Quan, G.-H. Chen, Adv. Funct. Mater. 20 (2010) 2165–2174.
[24] T. Yang, J. Xue, H. Tan, A. Xie, S. Li, W. Yan, Y. Shen, J. Mater. Chem. A 6 (2018) 1210–1218.

[25] Z. Luo, C. Li, D. Zhang, T. Wang, J. Gong, Chem. Commun. 52 (2016) 9013–9015.
[26] A. Sheikh, A. Yengantiwar, M. Deo, S. Kelkar, S. Ogale, Small 9 (2013) 2091–2096.
[27] T.W. Kim, K.-S. Choi, J. Physical Chemistry Letters 7 (2016) 447–451.
[28] D.P. Dubal, R. Holze, New J. Chem. 37 (2013) 403–408.
[29] K.J. McDonald, K.-S. Choi, Energy Environ. Sci. 5 (2012) 8553–8557.
[30] T.W. Kim, K.-S. Choi, Science 343 (2014) 990–994.
[31] S.S. Raut, B.R. Sankapal, Electrochim. Acta 198 (2016) 203–211.
[32] P. Guan, H. Bai, F. Wang, H. Yu, D. Xu, W. Fan, W. Shi, Chem. Eng. J. 358 (2019) 658–665.
[33] Y.-N. NuLi, Y.-Q. Chu, Q.-Z. Qin, J. Electrochem. Soc. 151 (2004) A1077–A1083.
[34] W. Cui, H. Bai, J. Shang, F. Wang, D. Xu, J. Ding, W. Fan, W. Shi, Electrochim. Acta 349 (2020), 136383.
[35] C. Miao, S. Ji, G. Xu, G. Liu, L. Zhang, C. Ye, ACS Appl. Mater. Interfaces 4 (2012) 4428–4433.
[36] S. Nakashima, K. Fujita, K. Tanaka, K. Hirao, T. Yamamoto, I. Tanaka, Physical Review B 75 (2007), 174443.
[37] N.D. Abazović, L. Mirenghi, I.A. Janković, N. Bibić, D.V. Šojić, B.F. Abramović, M. I. Čomor, Nanoscale Res. Lett. 4 (6) (2009) 518.
[38] X. She, Z. Zhang, Nanoscale Res. Lett. 12 (2017) 211.
[39] X.-T. Wang, Y. Li, X.-Q. Zhang, J.-F. Li, Y.-N. Luo, C.-W. Wang, Appl. Surf. Sci. (2019).
[40] X. Meng, L. Zhang, H. Dai, Z. Zhao, R. Zhang, Y. Liu, Mater. Chem. Phys. 125 (2011) 59–65.
[41] Z. Zhang, M. Wang, W. Cui, H. Sui, RSC Adv. 7 (2017) 8167–8177.
[42] Z.P. Chen, W.Q. Fang, B. Zhang, H.G. Yang, J. Alloy. Compd. 550 (2013) 348–352.
[43] L.-X. Pang, D. Zhou, Z.-M. Qi, W.-G. Liu, Z.-X. Yue, I.M. Reaney, J. Mater. Chem. C 5 (2017) 2695–2701.
[44] D. Zhou, L.-X. Pang, J. Guo, Z.-M. Qi, T. Shao, Q.-P. Wang, H.-D. Xie, X. Yao, C. A. Randall, Inorg. Chem. 53 (2014) 1048–1055.
[45] Z. Wang, D. Schiferl, Y. Zhao, H.S.C. O'Neill, J. Phys. Chem. Solids 64 (2003) 2517–2523.
[46] C.Y. Xu, P.X. Zhang, L. Yan, J. Raman Spectrosc. 32 (2001) 862–865.
[47] F. Deng, X. Lu, X. Pei, X. Luo, S. Luo, D.D. Dionysiou, J. Hazard. Mater. 332 (2017) 149–161.
[48] X. Wan, F. Niu, J. Su, L. Guo, PCCP 18 (2016) (1810) 31803.
[49] V. Théry, A. Boulle, A. Crunteanu, J.C. Orlianges, A. Beaumont, R. Mayet, A. Mennai, F. Cosset, A. Bessaudou, M. Fabert, Physical Review B 93 (2016), 184106.
[50] M.V. Malashchonak, E.A. Streltsov, D.A. Kuliomin, A.I. Kulak, A.V. Mazanik, Mater. Chem. Phys. 201 (2017) 189–193.
[51] R. Ameta, S.C. Ameta, Photocatalysis : principles and applications, CRC Press, Boca Ratón, Florida [etc.], 2018.
[52] A.N. Zulkifili, A. Fujiki, S. Kimijima, Applied Sciences 8 (2018) 216.
[53] Q. Yu, Z.-R. Tang, Y.-J. Xu, J. Energy Chemistry 23 (2014) 564–574.
[54] M.R.U.D. Biswas, W.-C. Oh, Solid State Sci. 80 (2018) 22–30.
[55] D. Verma, A.K. Kole, P. Kumbhakar, J. Alloy. Compd. 625 (2015) 122–130.
[56] S. Majumder, B.R. Sankapal, New J. Chem. 41 (2017) 5808–5817.
[57] T.W. Kim, Y. Ping, G.A. Galli, K.-S. Choi, Nat. Commun. 6 (2015) 8769.
[58] N.D. Quang, T.T. Hien, N.D. Chinh, D. Kim, C. Kim, D. Kim, Electrochim. Acta 295 (2019) 710–718.
[59] T.T. Hien, N.D. Quang, C. Kim, D. Kim, Nano Energy 57 (2019) 660–669.
[60] F.S. Hegner, I. Herraiz-Cardona, D. Cardenas-Morcoso, N. López, J.-R. Galán-Mascarós, S. Gimenez, ACS Appl. Mater. Interfaces 9 (2017) 37671–37681.
[61] W. Cui, J. Shang, H. Bai, J. Hu, D. Xu, J. Ding, W. Fan, W. Shi, Chem. Eng. J. 388 (2020), 124206.
[62] S. Majumder, P.K. Baviskar, B.R. Sankapal, Electrochim. Acta 222 (2016) 100–107.
[63] J.A. Seabold, K. Zhu, N.R. Neale, PCCP 16 (2014) 1121–1131.